Electronic Research Archive

https://www.aimspress.com/journal/era

ERA, 33(7): 4241–4258.
DOI: 10.3934/era.2025192
Received: 11 March 2025
Revised: 29 June 2025
Accepted: 08 July 2025
Published: 18 July 2025

Research article

Dynamic parallel MRI reconstruction via weighted nuclear norm plus sparse decomposition model

Lei Xue[1], **Benxin Zhang**[1] **and Jianqun Yang**[2,3,*]

[1] School of Electronic Engineering and Automation, Guilin University of Electronic Technology, Guilin, China

[2] Shenzhen Campus of Sun Yat-sen University, Shenzhen, China

[3] Shenzhen Institute of Advanced Technology, Shenzhen, China

* **Correspondence:** Email: yangjq65@mail.sysu.edu.cn.

Abstract: The dynamic parallel magnetic resonance imaging (MRI) reconstruction presents additional challenges due to the multi-coil acquisition process and an increase in data dimensions, which lead to a more ill-posed inverse problem compared to single coil dynamic MRI. Relevant optimization strategies usually involve solving the model after convex relaxation, which often leads to suboptimal solutions that either overshrink important signals or fail to adequately promote low-rankness and sparsity. In this paper, we propose a dynamic parallel MRI reconstruction model based on weighted nuclear norm and L_1 norm regularization in the framework of low-rank plus sparse (L+S) decomposition. The introduced weighted nuclear norm imposes nonuniform penalties on singular values and has a more flexible approximation to a low-rank property. To solve the resulting non-convex optimization problem, we employ the alternating direction method of multipliers (ADMM) based on variable splitting. The experimental results on multi-coil dynamic datasets show that this method provides a higher reconstruction quality than the traditional convex method.

Keywords: dynamic parallel magnetic resonance imaging; low-rank plus sparse decomposition; weighted nuclear norm; ADMM

1. Introduction

Magnetic resonance imaging (MRI) is an important medical research and diagnostic technique. However, the disadvantages of this technique include a long scanning time, which results in artifacts due to involuntary motion of the affected person, and additional noise disturbance, which affects the quality of the medical image reconstruction. Therefore, the key challenge in MRI research is to acquire clearer images in a shorter period of time. In clinical applications, the imaging time is shortened

by increasing either the main magnetic field strength or the gradient magnetic field strength and other related physical methods, which approaches their practical limits. Therefore, more effective mathematical techniques are needed to further accelerate image reconstruction.

The Compressed Sensing (CS) theory was first proposed by Candès [1], which states that if the signal is sparse in a certain transform domain, then it can be accurately reconstructed by sampling far below the Nyquist rate. Based on this theory, Lustig et al. first introduced it into the MRI field and proposed the compressive sensing MRI (CS-MRI) method [2]. This method exploits the sparsity of the image to achieve an effective undersampled MRI reconstruction, and further research began to focus on low-rank structures. Subsequently, Candes proposed a matrix completion model based on nuclear norm, which provided an effective convex optimization framework [3] for the low-rank matrix recovery problem. This method has become an important foundation for subsequent research on low-rank modeling. In order to better deal with the temporal redundancy information in high-dimensional medical image data, Jung et al. proposed the k-t FOCal Underdetermined System Solver (FOCUSS) [4], which is an algorithm that combines low-rank and sparse structures in dynamic MRI. Otazo et al. proposed the low-rank plus sparse decomposition model (L+S) [5], which combines low-rank matrix decomposition with sparse coding to effectively separate the background and dynamically change components in dynamic MRI. Based on the CS theory, combined with a low-rank sparse decomposition model [6–8], Candès proposed the robust principal component analysis (RPCA) [8], which forms a combination of the low-rank and sparse models. From this, Trémoulhéac [9] proposed the kt-RPCA method.

As an application of low-rank plus sparse decomposition in MRI reconstruction, researchers have found that although the original nondeterministic polynomial (NP)-hard problem is transformed into a convex optimization problem that is easy to solve, it is not enough to accurately characterize the low-rank structure. Considering the greater impact of larger singular values on the matrix approximation performance, Zhang et al. proposed the truncated nuclear norm model [10], which produced good recovery results in some scenarios. Gu et al. proposed the weighted nuclear norm minimization (WNNM) [11], which effectively improves the signal-to-noise ratio of an image while better preserving the image structure. With the continuous deepening of research on non-convex optimization, Lorenz et al. proposed sparse reconstruction methods based on nonconvex regularization, which have been shown to obtain better results than convex methods in many applications [12]. Subsequently, Lu et al. proposed the iteratively reweighted nuclear norm (IRNN) [13], where the low-rank structure of the matrix is better captured by weighting the nuclear norm to enhance the distinction between different singular values and the utilization of a priori information by the low-rank model.

Recent approaches have incorporated additional structural priors into the low-rank framework to improve the reconstruction accuracy. The advantages of models based on low-rank and sparse decompositions continue to this day. Shi et al. [14] proposed a low-rank and total variation (LRTV) regularization framework for magnetic resonance (MR) image super-resolution, which proved the efficiency of coupling spatial smoothing and low-rank constraint to solve the image super-resolution problem. The tensor-combined method effectively recovers high-dimensional images. He et al. [15] extended this idea to hyperspectral image restoration by introducing total variation regularized low-rank matrix factorization to recover the global low-rank structure while preserving spatial edges. Peng et al. [16] proposed an exact decomposition model that jointly captures low-rank, local smoothness, and sparsity, thus providing a more fine-grained structural decomposition framework. Based on this, Peng et al. [17] proposed a stable locally smooth principal component pursuit method with provable guarantees, which

improves the robustness to noise.

Dynamic parallel MRI combines the advantages of dynamic imaging and parallel sampling [18]: whether in the frequency domain [19, 20] or the image domain [21], employing a multicoil array to simultaneously acquire time-resolved data improves the sampling efficiency in the spatial domain and significantly accelerates the acquisition process. Compared with traditional single-coil MRI, parallel imaging can greatly reduce the data acquisition time without degrading the image quality. A notable work that combines dynamic parallel MRI and compressive sensing (sparsity) is k-t SPARSE-SENSE proposed by Otazo et al. [5]. The proposed method addresses the k-t SENSE problem by incorporating an additional sparsity prior, which is then extended by introducing a joint low-rank regularization alongside the sparsity prior and coil sensitivity information, thus leading to a low-rank based dynamic parallel imaging reconstruction framework. However, dynamic parallel MRI faces several challenges at the same time: first, the reconstruction problem is more ill-posed due to the significant increase in data dimensions; second, the modeling and correction of coil sensitivity increases the algorithmic complexity; and third, the dynamic structure in the time dimension is more complex, which requires more effective a priori modeling. Therefore, designing efficient mathematical models and optimization algorithms to improve the reconstruction quality of undersampled dynamic parallel MRI has become one of the core issues in current research. Fessler [22] proposed a variable splitting scheme (AL2) to process the model, which makes the L+S model more suitable for dynamic parallel multicoil MRI reconstruction.

The work in this paper aims to improve the quality of dynamic parallel MRI reconstruction. Inspired by the weighted nuclear norm, the non-convex penalty function is used to constrain the low-rank information. We propose a dynamic parallel MRI reconstruction model based on weighted nuclear norm and L_1-norm regularization in the framework of L+S decomposition. In experiments with dynamically under-sampled data from multiple coils, the proposed model enables further improvements in image quality and reconstruction efficiency.

2. Preliminary

2.1. The low-rank plus sparse model framework

In the reconstruction of dynamic MRI via the low-rank plus sparse model, assuming N_t images, each of which has a size of $N_x \times N_y$ dimensions. The matrix $X = [x_1, x_2, ..., x_{N_t}] \in \mathbb{C}^{N_x N_y \times N_t}$ is represented as a superposition of a low-rank matrix $L \in \mathbb{C}^{N_x N_y \times N_t}$ and a sparse matrix $S \in \mathbb{C}^{N_x N_y \times N_t}$, which is the result of vectorizing all time frames into a matrix:

$$X = L + S,$$

where L models the time-related background; it is naturally low-rank because the background part does not change over time and the information at the same location remains consistent across frames. S models the changing dynamic information over the background, which is naturally sparse. A finite dimensional spatio-temporal MRI model is as follows:

$$y = A(L + S) + \varepsilon,$$

where $y \in \mathbb{C}^{N_p}$ denotes the undersampled k-space undersampled data, $A \in \mathbb{C}^{N_x N_y \times N_t} \to \mathbb{C}^{N_p}$ is the sampling operation operator for MRI, and $\varepsilon \in \mathbb{C}^{N_p}$ is the noise.

To reconstruct X from the sampled data y, the following optimization problem can be constructed:

$$\begin{aligned} \min_{L,S} \quad & \text{rank}(L) + \|S\|_0 \\ \text{s.t.} \quad & \|A(L+S) - y\|_2 \le \varepsilon, \end{aligned}$$

where $\text{rank}(L)$ is the rank of the matrix L and $\|\cdot\|_0$ is the number of nonzero elements of the sparse matrix S. Solving this problem is NP-hard, and the classical L+S dynamic MR Image reconstruction model [23] that uses convex relaxation techniques is shown in (2.1). Under some unrelated assumptions, its corresponding reconstruction problem can be formulated as a convex optimization problem as follows:

$$\{L^*, S^*\} = \arg\min_{L,S}\{\frac{1}{2} \parallel A(L+S) - y \parallel_2^2 + \lambda_L \parallel L \parallel_* + \lambda_S \parallel \mathrm{T}S \parallel_1\}, \tag{2.1}$$

where $\|\cdot\|_*$ denotes the nuclear norm, which is defined as the sum of the singular values, and $\|\cdot\|_1$ denotes the L_1 norm, which is defined as the sum of the absolute values of the elements. In order to effectively extract these features, a sparsification transformation operator T is often introduced before the sparse term (such as Fourier, wavelet, gradient operator, and so on), whose purpose is to map S to a specific domain, thus making it have a stronger sparsity and facilitating constraints through L_1-norm regularization. λ_S, λ_L are given as balancing parameters for the three terms.

To minimize the optimization problem (2.1), two of the classic approaches are the iterative soft thresholding algorithm (ISTA) and the fast iterative soft thresholding algorithm (FISTA). Both of them are based on the proximal gradient method with proximal operators [24], and the latter introduces a momentum term in each step of its update, which allows for a faster convergence. Another main algorithm is based on the augmented lagrangian (AL) variable splitting method [25], which provides an efficient alternate direction method minimization (ADMM) for the L+S model. By introducing two new variables, P and Q, the convex optimization problem (2.1) can be written in the following constrained model:

$$\begin{aligned} &\arg\min_{L,S,P,Q} \frac{1}{2} \parallel A(L+S) - y \parallel_2^2 + \lambda_L \parallel P \parallel_* + \lambda_S \parallel Q \parallel_1 \\ &s.t. \begin{cases} P = L \\ Q = \mathrm{T}S. \end{cases} \end{aligned} \tag{2.2}$$

ADMM can be used to transform the problem into solving sub problems corresponding to P, Q, L, S to solve problem (2.2). Note that for the single-coil L+S dynamic MRI model, the above scheme update only requires solving a quadratic subproblem update of the coding operator A, which is shaped like a matrix $(A^*A + \delta I)^{-1}$. However, in the context of parallel multi-coil acquisitions, these methods incur a substantial computational overhead because the data processing operator A contains three additional pieces of information: the data acquisition operator Ω, the coil sensitivity C, and the Fourier coding operator Q, which produces $A = \Omega QC$. This composite operator reflects the standard acquisition model in dynamic parallel MRI.

2.2. Weighted nuclear norm regularization term

Assume $g_\lambda : R \to R^+$ is a continuous, nonconvex, and monotonically increasing function that may not be smooth in $[0, \infty]$. $\partial g_\lambda(X)$ the subgradient of a nonconvex function g_λ at X^k. λ is the regularization

coefficient, which is used to control the intensity. For every X, the following holds:

$$g_\lambda(X) \leq g_\lambda(X^k) + \partial g_\lambda(X^k)(X - X^k) = v^k X + C$$

where $v^k = \partial g_\lambda(X^k)$ denotes the set of all subgradients at X^k, and $C = g_\lambda(X^k) - \partial g_\lambda(X^k)X^k$ is a constant term independent of the variable.

Let $\sigma_1 \geq \sigma_2 \geq \cdots \geq \sigma_m$ be the singular values of matrix $X \in \mathbb{R}^{m\times n}$ (assumes $m \leq n$). We know that all existing non-convex penalty functions g_λ are convex and monotonically increasing on $[0, \infty]$, and their corresponding subgradients are monotonically decreasing functions that satisfy $0 \leq v_1 \leq v_2 \leq \cdots \leq v_m$. This property motivates us to set the gradient of the non-convex penalty function as the weight vector of the weighted nuclear norm, which allows for nonuniform penalties for singular values, and guarantees optimal low-rank recovery under ideal conditions, such as incoherence, that are difficult to satisfy. Moreover, this is particularly desirable when singular values have a physical interpretation, as is often the case in image and video data, where larger singular values often carry more important structural or temporal information [26]. By assigning smaller weights to larger singular values and larger weights to smaller singular values, the weighted nuclear norm achieves a closer approximation to the rank function, which enhances the robustness and expressiveness of low-rank modeling.

The expression of the weighted nuclear norm is as follows : $\|X\|_{*,w} = \sum_{i=1}^{m} w_i\sigma_i(X)$, where $\sigma_i(X)$ denotes the i-th singular value of the matrix X from the largest to the smallest. When the singular values are arranged in descending order, w_i is the increasing weight that corresponds to the singular values $\sigma_i(X)$, that is, $0 \leq w_1 \leq w_2 \leq ... \leq w_m$. The non-negative weight vectors $w = [w_1, ..., w_m]^T$ update formula is as follows:

$$w_i \in \partial g_\lambda(\sigma_i(X)). \tag{2.3}$$

[13] rigorously proved that the iteratively weighted nuclear norm can be equated to a convex quadratic programming problem by adding a proximal term to its linearization at X^k. Although the minimization problem of weighted nuclear norm is nonconvex and nonsmooth, it still has a globally optimal closed-form solution. For any $\lambda > 0$, the global optimal solution can be obtained from the weighted singular value threshold (WSVT) as follows:

$$X^* = U\mathcal{S}_{\lambda_{\omega_i}}(\Sigma)V^T.$$

Here, $Y \in R^{m\times n}$, $Y{=}U\Sigma V^T$ is the singular value decomposition of Y, $\mathcal{S}_{\lambda w_i}(\Sigma) = diag\{(\Sigma_i - \lambda w_i)_+\}$, and U, V stand for the orthogonal left singular matrix and the orthogonal right singular matrix after the singular value decomposition, respectively.

The weight function $g_\lambda(X)$ plays a central role in our regularization scheme. The selection of the weight functions $g_\lambda(X)$ are as shown in Table 1. There are some successful applications, including the Schatten-p quasinorm [27], L_p-norm ($0 < p < 1$), Capped-L1 [28], exponential penalty (ETP), smoothed clipped absolute deviation (SCAD) [29], minimally concave penalty (MCP) [12], Laplace [30], and so on. Since these functions differ in convexity and saturation, we will systematically evaluate their impact on the reconstruction quality in the experimental section.

Table 1. Popular nonconvex surrogate and corresponding weight function.

Penalty function	**function** $g_\lambda(X)$	**weight function**
Lp	λX^p	$p\lambda X^{1-p}$
Capped-L1	$\begin{cases}\lambda X, & \text{if } X < \gamma,\\ \lambda\gamma, & \text{if } X \geq \gamma.\end{cases}$	$\begin{cases}\lambda, & \text{if } X < \gamma,\\ [0,\lambda], & \text{if } X = \gamma,\\ 0, & \text{if } X > \gamma.\end{cases}$
ETP	$\frac{\lambda(1-\exp(-\gamma X))}{1-\exp(-\gamma)}$	$\frac{\lambda\gamma\exp(-\gamma X)}{1-\exp(-\gamma)}$
SCAD	$\begin{cases}\lambda X, & \text{if } X \leq \lambda,\\ -\frac{X^2+2\gamma\lambda X-\lambda^2}{2(\gamma-1)}, & \text{if } \lambda < X \leq \gamma\lambda,\\ \frac{\lambda^2(\gamma+1)}{2}, & \text{if } X > \gamma\lambda.\end{cases}$	$\begin{cases}\lambda, & \text{if } X \leq \lambda,\\ \frac{\gamma\lambda-X}{\gamma-1}, & \text{if } \lambda < X \leq \gamma\lambda,\\ 0, & \text{if } X > \gamma\lambda.\end{cases}$
MAP	$\begin{cases}\lambda X-\frac{X^2}{2\gamma}, & \text{if } X < \gamma\lambda,\\ \frac{1}{2}\gamma\lambda^2, & \text{if } X \geq \gamma\lambda.\end{cases}$	$\begin{cases}\lambda-\frac{X}{\gamma}, & \text{if } X < \gamma\lambda,\\ 0, & \text{if } X \geq \gamma\lambda.\end{cases}$
Laplace	$\lambda\left(1-\exp\left(-\frac{X}{\gamma}\right)\right)$	$\frac{\lambda}{\gamma}\exp\left(-\frac{X}{\gamma}\right)$

3. Weighted low-rank plus sparse dynamic parallel MRI reconstruction model

In this section, we consider the L+S reconstruction model for dynamic parallel MRI and the solution of its optimization model based on the variable splitting method. In dynamic parallel MRI, N_s is the total number of samples received from each receiving coil in all frames, N_c is the number of coils, N_x and N_y denote the image size of each frame, and N_t denotes the number of time frames. The nonconvex weighted low-rank plus sparse dynamic parallel MRI reconstruction model is as follows:

$$\underset{L,S}{\operatorname{argmin}}\frac{1}{2}\parallel \Omega QC(L+S)-y\parallel_2^2+\lambda_L\parallel L\parallel_{*,w}+\lambda_s\parallel \mathcal{F}_t(S)\parallel_1, \tag{3.1}$$

where Ω: $\mathbb{C}^{N_xN_yN_tN_c}\rightarrow\mathbb{C}^{N_sN_c}$ contains the undersampling pattern of all frames, C: $\mathbb{C}^{N_xN_y\times N_t}\rightarrow\mathbb{C}^{N_xN_yN_tN_c}$ represents the sensitivity map of the captured receiver coil and assuming that C is normalized such that $C^*C=I$, $Q\in\mathbb{C}^{N_xN_yN_tN_c\times N_xN_yN_tN_c}$ denotes the Fourier coding matrix, and $L,S\in\mathbb{C}^{N_xN_y\times N_t}$ is the desired dynamic image component. The sparse transformation operator adopted in this paper is the one-dimensional Fourier transform $\mathcal{F}_t$: $\mathbb{C}^{N_xN_y\times N_t}\rightarrow\mathbb{C}^{N_xN_yN_t}$ on the time axis and $\mathcal{F}_t(S)$=$(\mathcal{F}_t\otimes I_{N_sN_s})vec(S)$. The expression (3.1) is reformulated in a constrained form with the variable splitting method [22] as follows:

$$\begin{aligned}&\arg\min_{L,S,Z,X}\frac{1}{2}\parallel \Omega Z-d\parallel_2^2+\lambda_L\parallel L\parallel_{*,w}+\lambda_S\parallel \mathcal{F}_t(S)\parallel_1\\ &s.t.\begin{cases}Z=QCX\\ X=L+S.\end{cases}\end{aligned}$$

Its augmented Lagrangian function is as follows:

$$\begin{aligned}f(L,S,X,Z,\Lambda_1,\Lambda_2)=&\frac{1}{2}\parallel \Omega Z-d\parallel_2^2+\lambda_L\parallel L\parallel_{*,w}+\lambda_S\parallel \mathcal{F}_t(S)\parallel_1\\ &+\frac{\delta_1}{2}\parallel Z-QCX+\frac{\Lambda_1}{\delta_1}\parallel_2^2+\frac{\delta_2}{2}\parallel X-(L+S)+\frac{\Lambda_2}{\delta_2}\parallel_2^2,\end{aligned}$$

where δ_1, δ_2 are the Lagrangian penalty parameters and Λ_1, Λ_2 are the Lagrangian multipliers. For ease of writing, V_1, V_2 are used as Lagrange multiplier arrays, denoted respectively as follows:

$$V_1 = \frac{\Lambda_1}{\delta_2}, V_2 = \frac{\Lambda_2}{\delta_2}.$$

The L update involves the weighted nuclear norm, which is solved using weighted singular value thresholding (WSVT), where the threshold is computed based on dynamically adjusted weights as follows:

$$\begin{aligned} &\arg\min_L \lambda_L \|L\|_{*,w} + \frac{\delta_2}{2}\|X-(L+S)+V_2\|_2^2 \\ &= \arg\min_L \frac{\lambda_L}{\delta_2}\sum_{i=1}^{m} w_i\sigma_i(L) + \frac{1}{2}\|X-S+V_2-L\|_2^2. \end{aligned} \tag{3.2}$$

Therefore, L-subproblems can be solved by $L^* = U\mathcal{S}_{\frac{\lambda_L}{\delta_2}w}(X-S+V_2)V^T$. The weight vector w is dynamically updated by setting the weight vector to the gradient of the nonconvex function as shown in (2.3).

The S update contains a L_1 norm term that is solved using its proximity operator:

$$\begin{aligned} &\arg\min_S \lambda_S \parallel \mathcal{F}_t(S)\parallel_1 + \frac{\delta_2}{2}\parallel X-(L+S)+V_2\parallel_2^2 \\ &= \mathcal{F}_t^*(\arg\min_S \lambda_S \parallel \tilde{S}\parallel_1 + \frac{\delta_2}{2}\parallel \mathcal{F}_t(X-L+V_2)-\tilde{S}\parallel_2^2) \\ &= \mathcal{F}_t^* prox_{\frac{\lambda_S}{\delta_2}}(\mathcal{F}_t(X-L+V_2)); \end{aligned} \tag{3.3}$$

here, we use the fact that $\mathcal{F}_t$ is a unitary operator with the change of variables $\tilde{S} = \mathcal{F}_t(S)$.

The update of Z and X involve quadratic terms are easy to compute under this splitting method. For the update of the Z,

$$\begin{aligned} &\arg\min_Z \frac{1}{2}\parallel \Omega Z-d\parallel_2^2 + \frac{\delta_1}{2}\parallel Z-QCX+V_1\parallel_2^2 \\ &= (\Omega^*\Omega+\delta_1 I)^{-1}(\Omega^* d+\delta_1(QCX-V_1)). \end{aligned} \tag{3.4}$$

The under-sampled mask matrix can be expressed in the form of a Kronecker product. Then, $\Omega = I_{N_c}\otimes\tilde{\Omega}$ and

$$\Omega^*\Omega = (I_{N_c}\otimes\tilde{\Omega})(I_{N_c}\otimes\tilde{\Omega}) = I_{N_c}\otimes\tilde{\Omega}^*\tilde{\Omega}.$$

Note that $\tilde{\Omega}^*\tilde{\Omega}$ is a diagonal matrix; therefore, it is easy to calculate $(\Omega^*\Omega+\delta_1 I)^{-1}$.

For variables X, the update process is as follows:

$$\begin{aligned} &\arg\min_X \frac{1}{2}\parallel Z-QCX+V_1\parallel_2^2 + \frac{\delta_2}{2}\parallel X-(L+S)+V_2\parallel_2^2 \\ &= (C^*C+\frac{\delta_1}{\delta_2}I)^{-1}(C^*Q^*(Z+V_1)+\frac{\delta_2}{\delta_1}(L+S-V_2)) \\ &= \frac{\delta_1}{\delta_1+\delta_2}(C^*Q^*(Z+V_1)+\frac{\delta_2}{\delta_1}(L+S-V_2)). \end{aligned} \tag{3.5}$$

Here, we use the fact that Q is the unitary Fourier encoding matrix, and that $C^*C = I$ by assumption.

Iterative updates based on these subproblems complete the image reconstruction process. Algorithm 1 summarizes the implementation of these updates.

Algorithm 1

Inputs:

d: under-sampled multi-coil k-t data,
Ω: under-sampling mask,
Q: Fourier encoding operator,
C: coil sensitivity maps,
$\mathcal{F}_t$: temporal Fourier transform,
λ_L, λ_S: Regularization parameters of low-rank components and sparse components
δ_1, δ_2: penalty parameters,
k: iteration number.

Initialization:

$X_0 = L_0 = C^* Q^* \Omega^* d$, $S_0 = V_{1,0} = V_{2,0} = 0$, k=0 .

for $k = 1, 2, \ldots,$ **do**

The Z_{k+1} is calculated by (3.4),
The X_{k+1} is calculated by (3.5),
The L_{k+1} is calculated by (3.2),
The S_{k+1} is calculated by (3.3),
$V_{1,k+1} = V_{1,k} + (Z_{k+1} - QCX_{k+1})$,
$V_{2,k+1} = V_{2,k} + (X_{k+1} - L_{k+1} - S_{k+1})$,
$k \leftarrow k + 1$.

end for

Output: L_k, S_k.

4. Numerical experiments

In this section, we use two algorithms (ISTA, FISTA) and three models based on variable splitting ADMM (weighted low-rank plus TV sparse model WLTV, low-rank plus sparse model AL2, and the proposed weighted low-rank plus sparse model WLR) to verify the effect of the proposed model.

To compare the algorithms in a dynamic parallel MRI, experiments were performed using the Michigan Image Reconstruction Toolbox [31] with simulated coil sensitivity maps based on [32]. First, we used the physiologically improved nonuniform rational B-spline based Cardiac-Torso (PINCAT) phantom, which is a simulation dataset to test algorithms with adjustable parameters such as controllable noise, motion patterns, and so on. Next, experiments were validated on two publicly available dynamic MRI datasets: cardiac perfusion and cardiac cine. Each dataset consists of Cartesian undersampled multicoil data d, k-space undersampled mask Ω, and coil sensitivity maps C. We aimed to compare the algorithms and verify the efficiency of the new model on both datasets.

Experiments were conducted to assess the reconstruction quality using normalised error (NR) and the structural similarity index (SSIM), which are defined as follows:

$$\mathrm{NR} = \frac{\|X_k - X_{ture}\|_2}{\|X_k\|_2},$$

$$\mathrm{SSIM}(X_k, X_{true}) = \frac{(2\mu_{X_k}\mu_{X_{ture}})(2\sigma_{X_2X_{ture}} + C_2)}{(\mu_{X_2}^2 + \mu_{X_{ture}}^2 + C_1)(\sigma_{X_2}^2 + \sigma_{X_{ture}}^2 + C_2)},$$

where $X_k = L_k + S_k$ denotes the reconstructed image after iterations, and X_{ture} denotes full sampling data, $\mu_{(\cdot)}$ is the mean, $\sigma_{(*)}^2$ is the variance, and C_1, C_2 are constants with very small values to avoid cases where the denominator is zero.

4.1. The selection of the weight function

First, it should be noted that the non-convex functions mentioned, but not limited to those described in Table 1, can be applied to the reconstruction model (MRI) proposed in this paper as the weight function of the weighted nuclear norm. We applied different weight functions to the model. For both the comparison methods and the parameter settings of the non-convex functions, we respected the corresponding literature recommendations and appropriately adapted in order to give the best results. As shown in Table 2, we found that compared with functions such as SCAD and MCP, which have threshold or saturation behaviors, the L_p function shows good adaptability and robustness when applied to various types of datasets of different sizes. Moreover, the L_p function serves as a nonconvex surrogate that bridges the convex nuclear norm and the discontinuous rank function, thus providing a closer approximation to the true rank. Additionally, it leads to a simple and interpretable weight expression, which enables selective shrinkage of small singular values while preserving dominant components.

Table 2. Performance of different weighting functions in the experiment.

Image	**Weight function**	**parameter** ($\lambda = 1$)	**SSIM**	**NR (dB)**
Cardiac Perf	No weight	–	0.8744	0.1421
	L_p	$p = 0.5$	**0.8875**	**0.1359**
	Capped-L1	$\gamma = 10$	**0.9332**	**0.1104**
	ETP	$\gamma = 0.01$	**0.9013**	**0.1224**
	SCAD	$\gamma = 4.5$	0.8673	0.1501
	MCP	$\gamma = 6$	0.8683	0.1485
	Laplace	$\gamma = 10$	0.7466	0.2349
Cardiac Cine	No weight	–	0.9195	0.1023
	L_p	$p = 0.5$	**0.9377**	**0.0848**
	Capped-L1	$\gamma = 10$	**0.9546**	**0.0645**
	ETP	$\gamma = 0.1$	**0.9481**	**0.0709**
	SCAD	$\gamma = 3.7$	**0.9545**	**0.0645**
	MCP	$\gamma = 3$	**0.9305**	**0.0814**
	Laplace	$\gamma = 10$	0.7958	0.1722
PINCAT Phantom	No weight	–	0.9349	0.0879
	L_p	$p = 0.5$	**0.9811**	**0.0480**
	Capped-L1	$\gamma = 10$	**0.9713**	**0.0544**
	ETP	$\gamma = 0.1$	**0.9868**	**0.0416**
	SCAD	$\gamma = 3.7$	**0.9838**	**0.0466**
	MCP	$\gamma = 2$	**0.9762**	**0.0605**
	Laplace	$\gamma = 10$	**0.9719**	**0.0575**

The following experiments are based on the L_p function as a showcase. We chose to apply the L_p ($0 < p < 1$) function to the experimental part as a weighting function to demonstrate the model effect proposed in this paper. As shown in Table 3, $p = 0.8$ is the best value obtained after traversal $[0, 1]$.

Table 3. L_p-norm parameter selection of WLR.

	Cardiac Perfusion		Cardiac Cine		PINCAT Phantom	
p	NR(dB)	SSIM	NR(dB)	SSIM	NR(dB)	SSIM
0.1	0.308	0.636	0.200	0.745	0.079	0.936
0.2	0.231	0.753	0.176	0.788	0.072	0.947
0.3	0.176	0.830	0.146	0.841	0.065	0.957
0.4	0.144	0.874	0.114	0.895	0.058	0.967
0.5	0.135	0.887	0.084	0.937	0.052	0.975
0.6	0.132	0.892	0.064	0.960	0.047	0.979
0.7	0.120	0.903	0.063	0.957	0.046	**0.982**
0.8	**0.102**	**0.942**	**0.061**	0.960	**0.045**	0.982
0.9	0.109	0.933	**0.052**	**0.974**	0.050	0.977

4.2. The influence of the sparse operator

The sparse transformation operator adopted in this paper is the one-dimensional Fourier transform $\mathcal{F}_t$ on the time axis. This is because organ movements (such as heart rate and respiratory movements) [33] in dynamic MRI data often exhibit periodicity in time or low-frequency structures, which are more likely to show sparsity in the frequency domain. We visually demonstrate the influence of the Fourier transform operator used in this paper on the sparsity feature through the L_1 norm. Its existence is necessary to process the S component in this experiment, as shown in Table 4. Furthermore, the Fourier transform is a linear, reversible, and computationally efficient operation, which is suitable to be combined with the ADMM.

Table 4. Comparison of L_1-norms in spatial and temporal frequency domains.

	$\|.\|_1$	$\|\mathcal{F}_t(.)\|_1$	Decrease (%)
PINCAT Phantom	5.7908e+03	2.3154e+03	60.0
Cardiac Perfusion	1.1805e+05	4.7333e+04	59.9
Cardiac Cine	6.9202e+04	2.1958e+04	68.3

4.3. Parameter settings

The experiment is set up to match the data in the original code provided in literature [22]. For ISTA and FISTA, to ensure a fast convergence, we set the equilibrium parameters $\lambda_L = 0.01$ and $\lambda_S = 0.0025$. The step size t is 0.99 using ISTA and 0.5 for FISTA as provided by the convergence theory of those methods.

For AL methods, we adjust the penalty parameters of the ADMM by scanning $[0.01, 1]$ and selecting the values that achieve the fastest convergence among them. We observed that the model performance was relatively stable within the range, which indicates that this parameter had a relatively small influence on the convergence and reconstruction quality.

The proposed model includes two main regularization parameters, $\lambda_L$and λ_S, which control the

penalty strength for the low-rank and sparse terms, respectively. For different datasets, we adopt the cross-validation method for these two parameters to determine the optimal parameters, which will be specifically reflected in the following subsection, as shown in Figure 1.

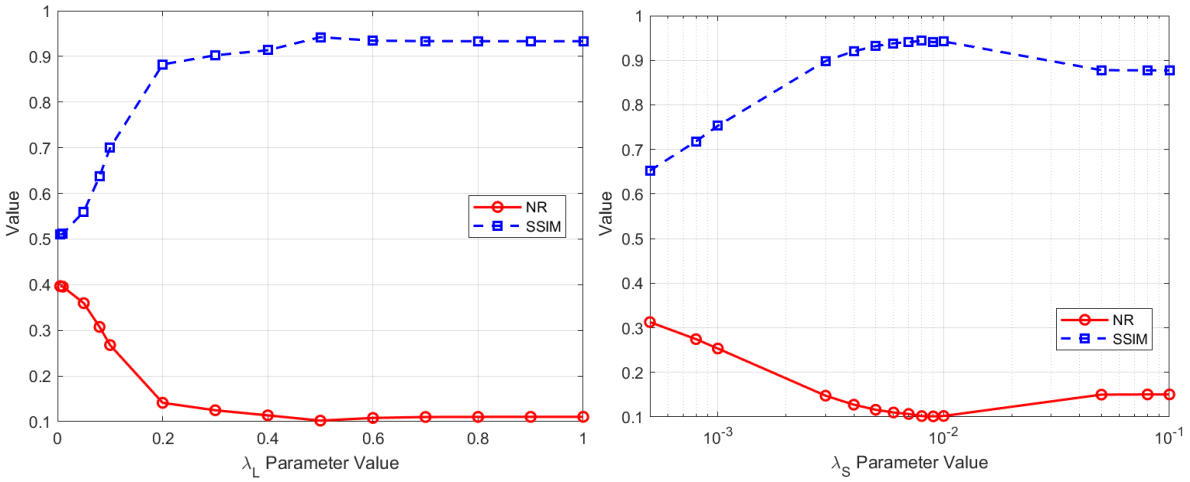

Figure 1. Dominant parameter optimization results for the cardiac perfusion data.

4.4. Experiment

The PINCAT phantom data used for the experiments had a spatial dimension of $N_x \times N_y = 128 \times 128$ images with 50 time frames. In the multi-coil setup, the coil sensitivity map was simulated with 32 coils and the number of coils was compressed to 8 coils. Zero-averaged Gaussian noise was added in the experiments to set the signal-to-noise ratio to 46 dB. The experiments validate the image reconstruction of algorithms under the different sampling acceleration factors adjusted by a pseudo-radial undersampling mask. The sampling acceleration factor F is defined as follows:

$$F = \frac{\text{Number of fully sampled lines}}{\text{The actual number of sampling lines}}.$$

It's worth mentioning that the reconstruction quality is closely related to the sampling acceleration factor. As the acceleration factor increases, the degree of undersampling becomes more severe, which makes the reconstruction problem more ill-posed and challenging. Generally speaking, the time consumption of the acquisition process decreases as the acceleration factor increases. The experiments were conducted using 5-bar per frame sampling, 10-bar sampling, and 15-bar sampling, which corresponded to acceleration factors of $128/5 \approx 25.6$, $128/10 \approx 12.8$, and $128/15 \approx 8.5$, respectively. The number of iterations was 40.

Figure 2 shows the 21st reconstruction frame on the PINCAT phantom image. As can be seen from the residual images, WLR shows better results in dynamic parallel MR image reconstruction under conditions of varying degrees of undersampling. Figure 3 provides a visualization of the two evaluation metrics with the number of iterations, where the proposed WLR consistently achieves a lower NR and higher SSIM scores across all acceleration settings. Table 5 shows the comparative performance of the different algorithms at different sampling rates on the PINCAT phantom data. The proposed WLR method yields visually superior reconstructions. It maintains clearer boundaries and

fewer artifacts, especially at high acceleration factors ($F = 25.6$), and verifies its applicability and advantages under high undersampling conditions.

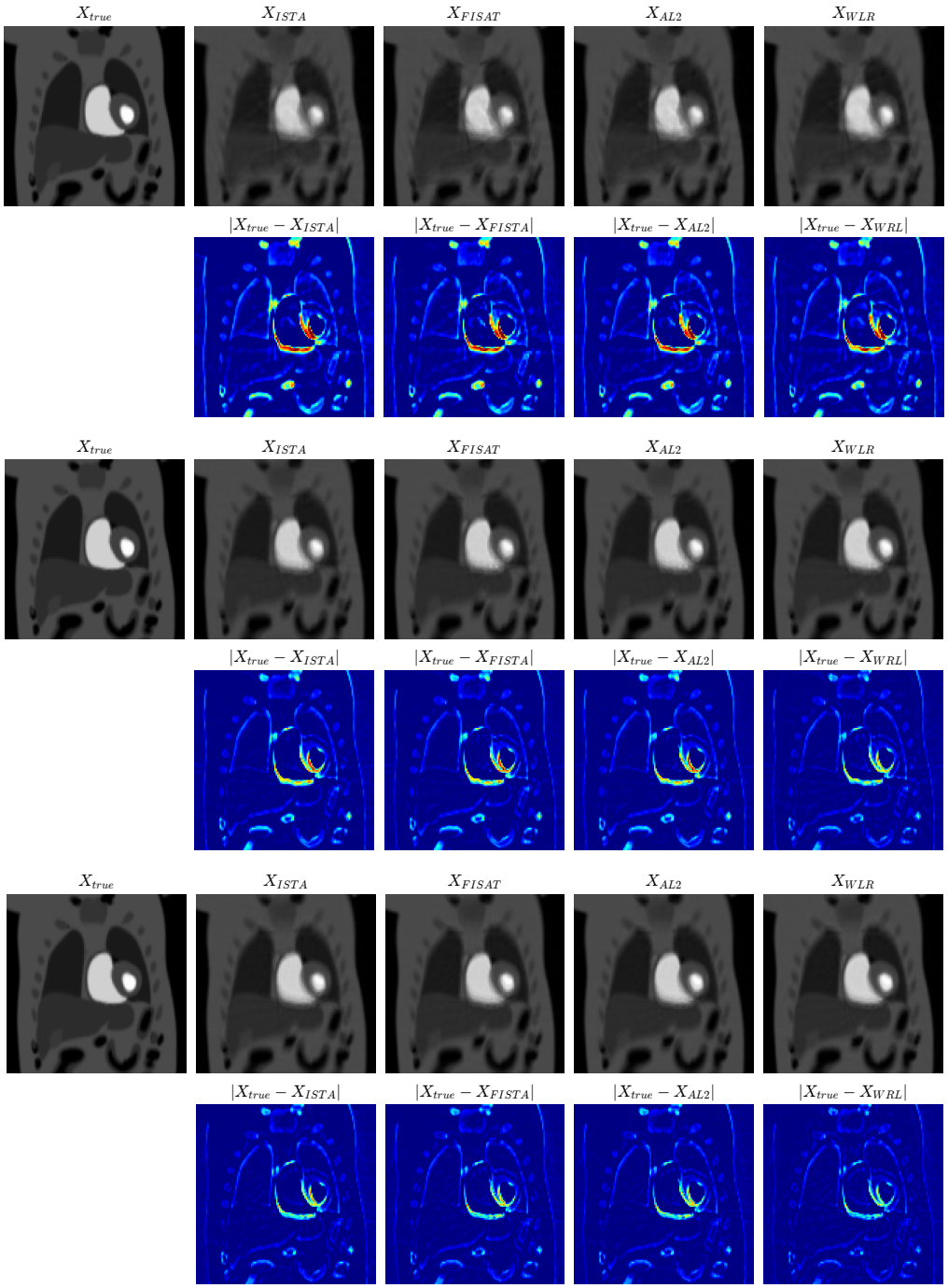

Figure 2. The first row of each group shows the reconstructed 21st frame PINCAT phantom images at acceleration factors of 25.6, 12.8, and 8.5 for the four algorithms. The second row shows the corresponding error images drawn at a scale of [0, 0.2].

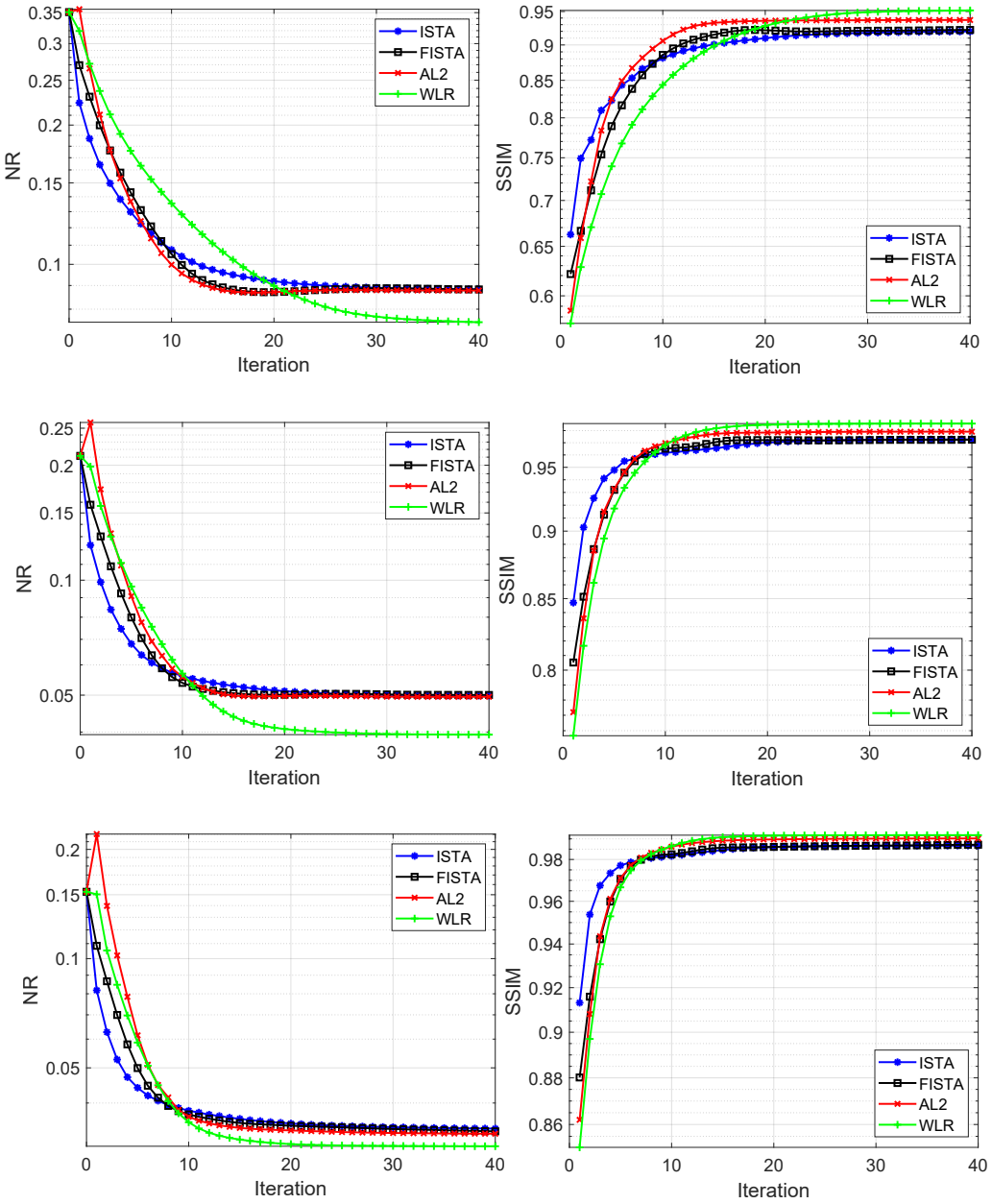

Figure 3. Errors in dynamic sequence reconstruction results and their structural similarity for the PINCAT phantom dataset at acceleration factors of 25.6 (first row), 12.8 (second row), and 8.5 (third row).

Experiments were performed on Cardiac perfusion and Cardiac cine datasets. The size of the cardiac perfusion dataset was $N_x \times N_y = 128 \times 128$, $N_t = 40$ and $N_c = 12$. For the variable splitting framework, $\lambda_L = 0.5$, and $\lambda_s = 0.01$. The cardiac cine dataset corresponds to images of size $N_x \times N_y = 256 \times 256$, and $N_t = 24, N_c = 12$. In this case, $\lambda_L = 0.15$, and $\lambda_S = 0.002$ were used.

Table 5. Performances of comparison algorithms at different acceleration factors for PINCAT phantom.

	F = 25.6		F = 12.8		F = 8.5	
Algorithm	NR	SSIM	NR	SSIM	NR	SSIM
ISTA	0.0883	0.7284	0.0498	0.9727	0.0340	0.9867
FISTA	0.0882	0.9221	0.0500	0.9724	0.0334	0.9871
AL2	0.0877	0.9370	0.0495	0.9791	0.0329	0.9902
WLR	**0.0749**	**0.9516**	**0.0394**	**0.9858**	**0.0304**	**0.9918**

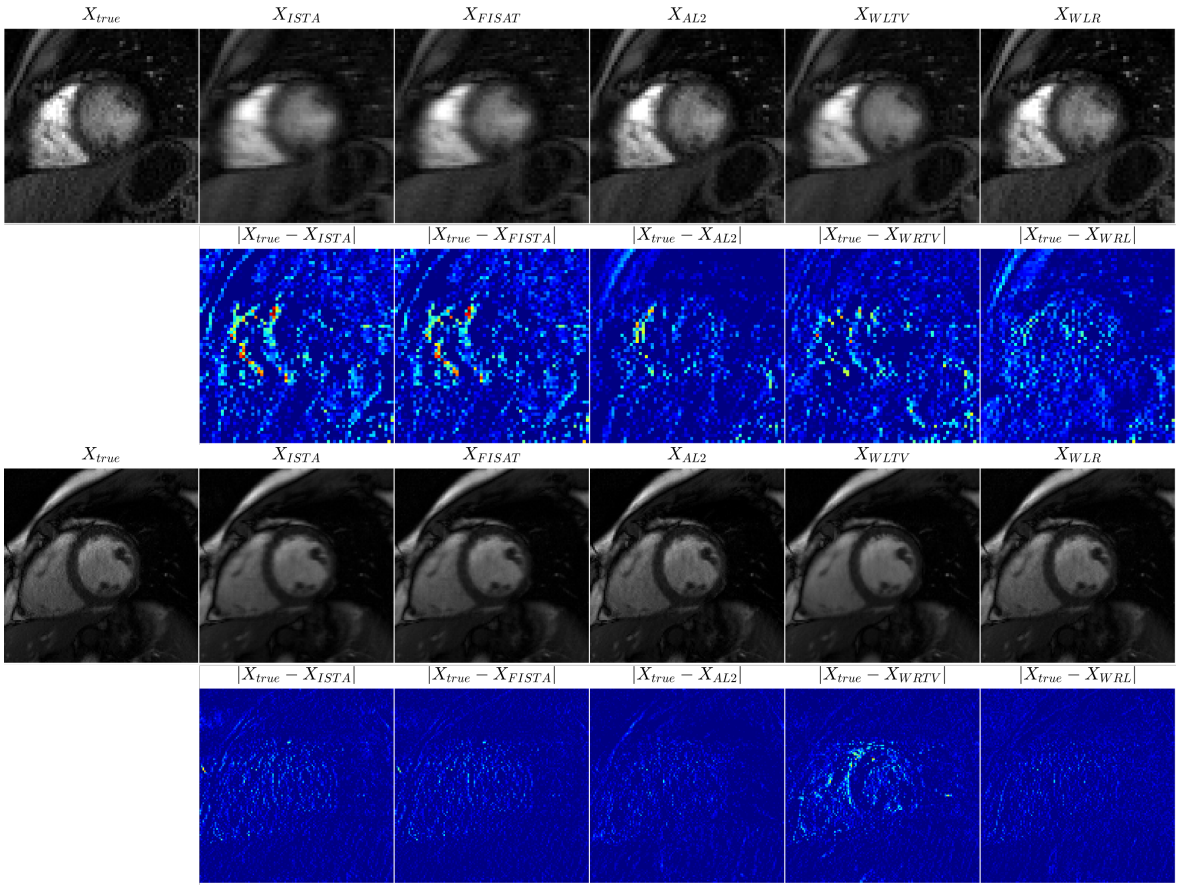

Figure 4. The first and second rows show the 8th reconstructed frame of the cardiac perfusion data and its residuals, while third and fourth rows show the 2nd reconstructed frame of the cardiac cinema data and its residuals.

Figure 4 shows the reconstructed images of two real datasets under different algorithms. The residual images show that the proposed WLR method achieves a finer reconstruction. As shown in Table 6, WLR consistently outperforms competing methods on both quantitative metrics, thus highlighting its potential. This further confirms that the proposed weighted low-rank regularization provides a more efficient reconstruction framework.

Table 6. Reconstruction results of cardiac perfusion and cardiac cine.

	Cardiac Perfusion		Cardiac Cine	
arithmetic	NR	SSIM	NR	SSIM
ISTA	0.2317	0.7284	0.0986	0.7284
FISTA	0.2080	0.7550	0.0773	0.9210
AL2	0.1173	0.9117	0.0657	0.9486
WLTV	0.1374	0.8934	0.0835	0.9480
WLR	**0.1022**	**0.9421**	**0.0612**	**0.9600**

4.5. Discussion

In recent years, deep learning–based methods have demonstrated outstanding performance in the reconstruction of undersampled dynamic MRI by incorporating implicit priors through neural networks. For example, Huang et al. [34] proposed a model-based low-rank plus sparse network (L+S-Net), which integrates deep neural networks with the low-rank and sparse decomposition frameworks. The L+S network is defined through an iterative process based on the alternating linearization minimization. The method achieved a SSIM up to 0.9849 on the cardiac cine dataset under an acceleration factor of 12, which significantly outperformed the SSIM 0.9600 obtained by our current optimization-based model under an 8-fold acceleration on the same dataset. However, it should be pointed out that compared with deep learning based methods, our proposed does not require training data and training processing.

Deep learning has been widely used in single-coil dynamic image reconstruction. However, as far as we know, it is still in the development stage in the direction of dynamic parallel MRI reconstruction. Fortunately, our proposed optimization framework itself has a good compatibility and scalability, whether combined with other regularization terms or implicit prior information based on deep learning. In the future, we will work on fusing the optimization model prior with the deep learning structure to further improve the reconstruction effect and performance of dynamic parallel MRI.

5. Conclusions

In this paper, we proposed a weighted low-rank plus sparse model to reconstruct dynamic parallel MRI. The weighted nuclear norm was able to enhance the low-rank structure of the image in a more flexible way and effectively overcame the shortcomings of the traditional nuclear norm in the reconstruction accuracy. The experimental results showed that the quality of the reconstructed image was effectively improved under high under-sampling conditions, and proved the effectiveness of the proposed model in capturing the low-rank structure of the image. In addition, further validations on different types of applications are helpful for the popularization of new model. The introduction of more complex spatial or spatio-temporal regularities will be further explored in the future to cope with the reconstruction challenges at lower sampling rates.

Use of AI tools declaration

The authors declare they have not used Artificial Intelligence (AI) tools in the creation of this article.

Conflict of interest

The authors declare that they have no competing interests.

Acknowledgments

This work was supported in part by the National Natural Science Foundation of China under Grant No. 62171147, in part by Guangxi Natural Science Foundation under Grant No. 2024GXNSFAA010512 and GUIKEAB25069275, and in part by Shenzhen Science and Technology Program under Grant No. JCYJ20210324102204012.

References

1. E. J. Candès, J. Romberg, T. Tao, Robust uncertainty principles: Exact signal reconstruction from highly incomplete frequency information, *IEEE Trans. Inf. Theory*, **52** (2006), 489–509. https://doi.org/10.1109/TIT.2005.862083
2. M. Lustig, D. Donoho, J. M. Santos, J. M. Pauly, Compressed sensing MRI, *IEEE Signal Process. Mag.*, **25** (2008), 72–82. https://doi.org/10.1109/MSP.2007.914728
3. E. J. Candès, B. Recht, Exact matrix completion via convex optimization, *Found. Comput. Math.*, **9** (2009), 717–772. https://doi.org/10.1007/s10208-009-9045-5
4. H. Jung, K. Sung, K. S. Nayak, E. Y. Kim, J. C. Ye, k-t FOCUSS: A general compressed sensing framework for high resolution dynamic MRI, *Magn. Reson. Med.*, **61** (2009), 103–116. https://doi.org/10.1002/mrm.21757
5. R. Otazo, D. Kim, L. Axel, D. K. Sodickson, Combination of compressed sensing and parallel imaging for highly accelerated first-Pass cardiac perfusion MRI, *Magn. Reson. Med.*, **64** (2010), 767–776. https://doi.org/10.1002/mrm.22463
6. E. J. Candès, M. B. Wakin, An introduction tocompressive sampling, *IEEE Signal Process. Mag.*, **25** (2008), 21–30. https://doi.org/10.1109/MSP.2007.914731
7. D. L. Donoho, Compressed sensing, *IEEE Trans. Inf. Theory*, **52** (2006), 1289–1306. https://doi.org/10.1109/TIT.2006.871582
8. E. J. Candès, X. Li, Y. Ma, J. Wright, Robust principal component analysisl, *J. ACM*, **58** (2011), 1–37. https://doi.org/10.1145/1970392.1970395
9. B. R. Trémoulhéac, *Low-Rank and Sparse Reconstruction in Dynamic Magnetic Resonance Imaging via Proximal Splitting Methods*, PhD theis, University College London, 2015.
10. D. B. Zhang, Y. Hu, P. Ye, X. Li, X. He, Matrix completion by truncated nuclear norm regularization, in *2012 IEEE Conference on Computer Vision and Pattern Recognition*, (2012), 3414–3421. https://doi.org/10.1109/CVPR.2012.6247927
11. S. Gu, Q. Xie, D. Meng, W. Zuo, X. Feng, L. Zhang, Weighted nuclear norm minimization and its applications to low level vision, *Int. J. Comput. Vision*, **121** (2017), 183–208. https://doi.org/10.1007/s11263-016-0930-5

12. T. Ince, A. Nacaroglu, N. Watsuji, Nonconvex compressed sensing with partially known signal support, *Signal Process.*, **93** (2013), 344–348. https://doi.org/10.1016/j.sigpro.2012.07.011

13. C. Lu, J. Tang, S. Yan, Z. Lin, Generalized nonconvex nonsmooth low-rank minimization, in *Proceedings of the IEEE Conference on Computer Vision and Pattern Recognition*, (2014), 4130–4137.

14. F. Shi, J. Cheng, L. Wang, P. Yap, D. Shen, LRTV: MR image super-resolution with low-rank and total variation regularizations, *IEEE Trans. Med. Imaging*, **34** (2015), 2456–2466. https://doi.org/10.1109/TMI.2015.2437894

15. W. He, H. Zhang, L. Zhang, H. Shen, Total-variation-regularized low-rank matrix factorization for hyperspectral image restoration, *IEEE Trans. Geosci. Remote Sens.*, **54** (2015), 178–188. https://doi.org/10.1109/TGRS.2015.2452812

16. J. Peng, Y. Wang, H. Zhang, J. Wang, D. Meng, Exact decomposition of joint low rankness and local smoothness plus sparse matrices, *IEEE Trans. Pattern Anal. Mach. Intell.*, **45** (2022), 5766–5781. https://doi.org/10.1109/TPAMI.2022.3204203

17. J. Peng, H. Wang, X. Cao, X. Jia, H. Zhang, D. Meng, Stable local-smooth principal component pursuit, *SIAM J. Imaging Sci.*, **17** (2024), 1182–1205. https://doi.org/10.1137/23M1580164

18. Z. Hu, C. Zhao, X. Zhao, L. Kong, J. Yang, X. Wang, et al., Joint reconstruction framework of compressed sensing and nonlinear parallel imaging for dynamic cardiac magnetic resonance imaging, *BMC Med. Imaging*, **21** (2021). https://doi.org/10.1186/s12880-021-00685-2

19. D. K. Sodickson, W. J. Manning, Simultaneous acquisition of spatial harmonics (SMASH): Fast imaging with radiofrequency coil arrays, *Magn. Reson. Med.*, **38** (1997), 591–603. https://doi.org/10.1002/mrm.1910380414

20. M. A. Griswold, P. M. Jakob, R. M. Heidemann, M. Nittka, V. Jellus, J. Wang, et al., Generalized autocalibrating partially parallel acquisitions (GRAPPA), *Magn. Reson. Med.*, **47** (2002), 1202–1210. https://doi.org/10.1002/mrm.10171

21. K. P. Pruessmann, M. Weiger, M. B. Scheidegger, P. Boesiger, SENSE: Sensitivity encoding for fast MRI, *Magn. Reson. Med.*, **42** (1999), 952–962. https://doi.org/10.1002/(SICI)1522-2594(199911)42:5<952::AID-MRM16>3.0.CO;2-S

22. C. Y. Lin, J. A. Fessler, Efficient dynamic parallel MRI reconstruction for the low-rank plus sparse model, *IEEE Trans. Comput. Imaging*, **39** (2020), 17–26. https://doi.org/10.1109/TCI.2018.2882089

23. R. Otazo, E. Candès, D. K. Sodickson, Low-rank plus sparse matrix decomposition for accelerated dynamic MRI with separation of background and dynamic components, *Magn. Reson. Med.*, **73** (2015), 1125–1136. https://doi.org/10.1002/mrm.25240

24. B. Gu, D. Wang, Z. Huo, H. Huang, Inexact proximal gradient methods for non-convex and non-smooth optimization, in *Proceedings of the AAAI Conference on Artificial Intelligence*, (2018), 3093–3100. https://doi.org/10.1609/aaai.v32i1.11802

25. Z. Lin, M. Chen, Y. Ma, The augmented Lagrange multiplier method for exact recovery of corrupted low-rank matrices, preprint, arXiv:1009.5055. https://doi.org/10.48550/arXiv.1009.5055

26. S. Xu, J. Zhang, L. Bo, H. Li, H. Zhang, Z. Zhong, et al., Singular vector sparse reconstruction for image compression, *Comput. Electr. Eng.*, **91** (2021), 107069. https://doi.org/10.1016/j.compeleceng.2021.107069
27. Y. Xie, S. Gu, Y. Liu, W. Zuo, W. Zhang, L. Zhang, Weighted schatten p-norm minimization for image denoising and background subtraction, *IEEE Trans. Image Process.*, **250** (2016), 4842–4857. https://doi.org/10.1109/TIP.2016.2599290
28. M. Chen, Q. Wang, S. Chen, X. Li, Capped l_1-norm sparse representation method for graph clustering, *IEEE Access*, **7** (2019), 54464–54471. https://doi.org/10.1109/ACCESS.2019.2912773
29. J. Fan, R. Li, Variable selection via nonconcave penalized likelihood and its oracle properties, *J. Am. Stat. Assoc.*, **96** (2001), 1348–1360. https://doi.org/10.1198/016214501753382273
30. J. Trzasko, A. Manduca, Highly undersampled magnetic resonance image reconstruction via homotopic L_0-minimization, *IEEE Trans. Med. Imaging*, **28** (2009), 106–121. https://doi.org/10.1109/TMI.2008.927346
31. *Michigan Image Reconstruction Toolbox (MIRT)*, 2018. Available from: http://web.eecs.umich.edu/fessler/code.
32. M. I. Grivich, D. P. Jackson, The magnetic field of current-carrying polygons: An application of vector field rotations, *Am. J. Phys.*, **68** (2000), 469–474. https://doi.org/10.1119/1.19461
33. R. Otazo, E. Candès, D. K. Sodickson, Low rank plus sparse matrix decomposition for accelerated dynamic MRI with separation of background and dynamic components, *Magn. Reson. Med.*, **73** (2015), 1125–1136. https://doi.org/10.1002/mrm.25240
34. W. Huang, Z. Ke, Z. X. Cui, J. Cheng, Z. Qiu, S. Jia, et al., Deep low-rank plus sparse network for dynamic MR imaging, *Med. Image Anal.*, **73** (2021), 102190. https://doi.org/10.1016/j.media.2021.102190

AIMS Press